International Journal of Heat and Mass Transfer 51 (2008) 5562–5577

Contents lists available at ScienceDirect

International Journal of Heat and Mass Transfer

journal homepage: www.elsevier.com/locate/ijhmt

Numerical predictions of submicrometer aerosol deposition in the nasal cavity using a novel drift flux approach

Jinxiang Xi [a], P. Worth Longest [a,b,*]

[a] Department of Mechanical Engineering, Virginia Commonwealth University, 601 West Main Street, P.O. Box 843015, Richmond, VA 23284-3015, United States
[b] Department of Pharmaceutics, Virginia Commonwealth University, Richmond, VA, United States

ARTICLE INFO

Article history:
Received 2 November 2007
Received in revised form 4 April 2008
Available online 13 June 2008

Keywords:
Respiratory particle dynamics
Respiratory dosimetry
Microdosimetry
Health effects of submicrometer aerosols
Respiratory drug delivery
Drift flux model
Nasal deposition of fine and ultrafine aerosols

ABSTRACT

Evaluating the health effects of inhaled submicrometer aerosols, such as combustion particulate matter and bioaerosols, requires a thorough understanding of transport and deposition in the nasal airway. However, numerical simulations of fine respiratory aerosols (100–1000 nm) remain challenging due to low deposition fractions and the action of concurrent inertial and diffusive deposition mechanisms. The objective of this study was to evaluate the transport and deposition of submicrometer aerosols in the nasal cavity based on a novel drift flux model with a near-wall velocity correction (DF-VC), which accounts for the effects of particle inertia and diffusion. Deposition results were also obtained for a commonly implemented chemical species (CS) model that only accounts for particle diffusion. The nasal cavity geometry was developed based on available MRI data, which has also been used in the previous experimental studies. Particle sizes ranging from 1 nm through 1000 nm and inhalations flow rates covering 4–30 L/min were considered. Under these conditions, turbulence only appeared significant in the nasal vestibule-valve region and the dorsal portion of the nasopharynx. In contrast, most of the main nasal passage appeared to have primarily laminar flow. Simulation results of the novel DF-VC model were shown to provide a good match to experimental deposition values from various nasal replica casts, and corroborated an existing empirical correlation for *in vivo* nasal deposition of submicrometer aerosols. Comparisons of the DF-VC and CS models indicated that inertial effects began to significantly influence total deposition in the nasal cavity at particle Stokes numbers greater than a critical value of $St_k = 1.0 \times 10^{-5}$, which is equivalent to a 90 nm particle under resting conditions and a 50 nm aerosol during moderate activity. A new correlation for mass transfer and deposition in the nasal airways was proposed that accounts for both inertial and diffusional deposition mechanisms and can be applied for all submicrometer aerosols. Results of this study indicate that a drift flux particle transport model with near-wall velocity corrections can provide an effective approach in simulating the transport and deposition of submicrometer respiratory aerosols in human nasal airways.

1. Introduction

The transport and deposition of submicrometer aerosols in the nasal cavity may have significant effects on human health. Submicrometer aerosols include particle sizes in the fine (1 μm to 100 nm) and ultrafine (<100 nm) regimes. Current studies indicate that fine and especially ultrafine particulate matter may be more biologically active and potentially more toxic than micrometer particles of the same material [1–4]. Sources of submicrometer aerosols include diesel exhaust in the nuclei (5–50 nm) and accumulation (50–500 nm) modes [5], cigarette smoke (140–500 nm) [6,7], and radioactive decay (1–200 nm) [8]. Submicrometer bioaerosols include respiratory specific viruses such as Avian flu and SARS, which typically range from 20 to 200 nm [9]. Negative health effects associated with the inhalation and deposition of submicrometer aerosols include nasal carcinomas [10] in the case of radioactive particles and combustion byproducts. Nasal deposition of bioaerosols can lead to the spread of infectious diseases.

In contrast with potentially negative health effects, a number of pharmaceutical aerosols are currently being developed for nasal delivery. For the most part, pharmaceutical aerosols intended for nasal delivery are larger than approximately 20 μm to minimize penetration into the lungs [11,12]. However, the delivery of submicrometer particles to the nasal geometry may have the advantages of increased absorption rates, improved bioavailability, and prolonged periods of action. Furthermore, pharmaceutical submicrometer aerosols may better target the uppermost part of the

* Corresponding author. Address: Department of Mechanical Engineering, Virginia Commonwealth University, 601 West Main Street, P.O. Box 843015, Richmond, VA 23284-3015, United States. Tel.: +1 804 827 7023; fax: +1 804 827 7030.
E-mail address: pwlongest@vcu.edu (P.W. Longest).

0017-9310/$ - see front matter © 2008 Elsevier Ltd. All rights reserved.
doi:10.1016/j.ijheatmasstransfer.2008.04.037

nasal cavity [13], which is referred to as the olfactory region, where direct absorption into the brain is possible. The deposition of inhaled medications in the olfactory region may be used to more effectively treat disorders of the central nervous system, such as Parkinson's and Alzheimer's diseases [14,15].

A number of *in vitro* and *in vivo* studies have considered the deposition of submicrometer aerosols in the nasal cavity. Experimental *in vitro* studies that have evaluated the nasal deposition of ultrafine aerosols in humans include Cheng et al. [16] and Swift and Strong [17]. The study of Cheng et al. [16] considered the deposition of ultrafine aerosols ranging from 4 to 150 nm in 10 subjects and quantified variability in nasal geometries using MRI scans. Deposition was shown to be a function of nasal cavity surface area, minimum cross-sectional area, and shape complexity. A correlation for nasal deposition was developed as a function of geometric parameters and particle diffusion. As a result, it was concluded that nasal deposition of ultrafine aerosols was highly variable among subjects and depended largely on the diffusional transport mechanism. A common disadvantage of *in vivo* experimental methods for nasal deposition studies is difficulty in determining local deposition values. Imaging methods have become available that can resolve general regions of particle deposition within the nasal cavity [18]. However, these methods have not been applied to the deposition of submicrometer aerosols in the nasal airways. Furthermore, no experimental *in vivo* data is available for the deposition of fine respiratory aerosols ranging from approximately 200 nm to 1 μm in the nasal cavity.

In vitro studies of submicrometer aerosol transport and deposition provide the advantage of avoiding human subject testing and can be used to determine deposition within general regions of the nasal cavity. A number of experimental studies have considered deposition of ultrafine aerosols in replicas of the human nose [19–25]. The nasal geometries used in these studies are typically derived from medical scan data (CT and MRI) or casts of cadavers. Results of the available *in vitro* experiments are in general agreement with the deposition data from *in vivo* studies for ultrafine aerosols [16]; however, less dependence on flow rate is often observed in the *in vitro* measurements [26]. Based on a collection of *in vivo* nasal deposition studies, Cheng et al. [26] suggested a best-fit correlation for particle sizes less than 150 nm. Later, Cheng [19] incorporated *in vivo* and *in vitro* nasal deposition data of ultrafine and micrometer particles to develop a correlation for particle sizes in the diffusional and the impaction deposition regimes.

In a series of *in vitro* studies, Kelly et al. [27,24] evaluated the effects of surface roughness in replica models of the nasal cavity constructed from two different manufacturing techniques on the deposition of ultrafine and micrometer particles. The deposition of ultrafine particles less than approximately 150 nm was not found to be significantly affected by surface roughness characteristics. As a result, it was concluded that ultrafine aerosols deposit primarily by diffusion in the nasal airway. As with *in vivo* experiments, current *in vitro* models have also generally neglected the deposition of fine aerosol in the range of 200 nm through approximately 1 μm.

Previous numerical studies have considered the transport and deposition of fine and ultrafine particles in the nasal cavity [28–30,13,31,32]. Similar CFD studies have also evaluated the transport and absorption of dilute chemical species in the nasal passages [33–35]. Comparisons of CFD results to experimental deposition data for submicrometer aerosols in the nasal airways are often difficult due to differences in the geometric models and the complexity of the transport dynamics. Martonen et al. [29] developed a numerical model of ultrafine aerosol transport and deposition in the nasal cavity based on diffusional theory in a highly simplified tubular geometry. The resulting correlation agreed well with experimental predictions of total deposition for nanoparticles ranging from 1 to 100 nm. Recently, Shi et al. [13] reported local deposition patterns of very small nanoparticles in the nasal cavity under laminar and transient breathing conditions. Zamankhan et al. [32] simulated the transport and deposition of ultrafine aerosols in the range of 1–100 nm and showed good agreement with the *in vivo* deposition data of Cheng et al. [16] for particles less than approximately 20 nm. However, particles greater than 20 nm did not match the experimental data to a high degree. Liu et al. [28] simulated particles ranging from 0.354 to 16 μm using three Lagrangian particle tracking models. Results of this study showed that the standard eddy interaction model used for Lagrangian particle tracking in turbulent flows significantly over predicted the deposition of the smaller particles considered.

As described above, a number of previous experimental and numerical studies have considered the transport and deposition of ultrafine aerosols in the nasal cavity. However, respiratory deposition data for particles in the range of fine aerosols (100–1000 nm) is scarce. Furthermore, no available studies have reported the local deposition of fine respiratory aerosol in the nasal cavity. In general, previous studies may have largely neglected the deposition of fine respiratory aerosols in the nasal airways due to expected low deposition rates. However, this size regime contains many potentially toxic aerosols, as described above, including some respiratory viruses, diesel exhaust and tobacco smoke aerosols, and larger radioactive decay byproducts. These aerosols will deposit in the nose in perceivable amounts and may have significant local and systemic health effects.

Numerical simulations of fine respiratory aerosols are challenging due to low deposition efficiencies and the action of concurrent inertial and diffusive deposition mechanisms [36]. Previous studies of submicrometer aerosol transport and deposition in the nasal–oral region have typically employed either a Eulerian [13,37,31] or a Lagrangian [38,32] representation of the particle phase. The chemical species (CS) Eulerian model that is typically applied for ultrafine aerosols is highly efficient and shows excellent agreement with analytic solutions for diffusive deposition in a tubular geometry, where inertia does not influence deposition [36,13,39]. However, the CS Eulerian model that is typically used for respiratory aerosols neglects the effects of finite particle inertia [40,36]. Longest and Xi [36] have shown that inertia may significantly affect the total deposition of submicrometer aerosols as small as 70 nm and the local deposition of 40 nm particles in a bifurcating respiratory model. Furthermore, Longest and Xi [38] showed that the Eulerian model does not account for increased residence times associated with ultrafine aerosols in the range of 1 to 5 nm.

In contrast with the Eulerian model that is typically used for respiratory aerosols, Lagrangian particle tracking does account for both diffusive and inertial forces [36]. The primary disadvantage of Lagrangian particle tracking is that it results in a stiff set of equations for fine and ultrafine particles, which is difficult to solve. As a result, small time steps must be implemented in conjunction with a stiff equation solver. Furthermore, the Lagrangian model may require an excessive number of particles to resolve regional and especially local deposition characteristics.

To improve the simulation of submicrometer aerosols in the respiratory tract, Longest and Oldham [41] proposed and tested a novel drift flux model and evaluated deposition predictions using comparisons with experimental *in vitro* data. In evaluating this model, regional and local deposition results were considered for the deposition of 400 nm and 1 μm particles in a symmetric idealized double bifurcation model. Implementation of a standard drift flux approach to account for particle inertia [42,40,43] was found to over predict particle deposition by approximately one order of magnitude. This over estimation of deposition was because of the rapid deceleration of submicrometer aerosols in the near-wall region, which could not be resolved on a continuous basis with a practical computational grid. As an alternative, a continuous-field

drift flux model was developed by Longest and Oldham [41] that included a sub-grid near-wall Lagrangian solution for particle inertia. The resulting hybrid drift flux velocity correction (DF-VC) model provided a good match to experimental deposition values on a regional and highly localized basis. Specifically, the DF-VC model matched total experimental deposition results to within 10% for both 400 nm and 1 μm particles in an idealized double bifurcation model. Considering the highly local deposition of fine aerosols, the DF-VC model matched the experimentally determined elevated contours at the first and second bifurcations for both 400 nm and 1 μm particles. Furthermore, the DF-VC model significantly reduced the time required for a steady state deposition simulation compared with a standard Lagrangian solution.

The objective of this study is to evaluate the transport and deposition of submicrometer aerosols in the nasal cavity based on a novel drift flux model with a near-wall velocity correction (DF-VC). The drift flux approximation accounts for deposition due to both diffusion and finite particle inertia in laminar and turbulent flow fields. Deposition results are compared with a standard chemical species (CS) model, which is frequently implemented for submicrometer aerosols, but neglects particle inertia. Differences in the DF-VC and CS predictions are used to evaluate the relative effects of finite particle inertia on the local and regional deposition of ultrafine and fine respiratory aerosols in the nasal cavity. Regional deposition results of the DF-VC model are also compared with available *in vivo* and *in vitro* data. This study develops a deposition correlation that accounts for both inertial and diffusive transport mechanisms and is applicable to both fine and ultrafine submicrometer respiratory aerosols.

2. Methods

The focus of this study is to assess the performance of a novel drift flux approximation (DF-VC) and the standard chemical species model (CS) for simulating the deposition of submicrometer aerosols in the nasal passages. Comparisons of numerical results are made with previously determined *in vitro* and *in vivo* deposition data. To facilitate these comparisons, an anatomically realistic nasal airway model has been constructed based on MRI images of a living healthy subject. Expected flow regimes ranging from laminar through turbulent flow (i.e., 4–30 L/min) are considered for both ultrafine (1–100 nm) and fine (100–1000 nm) monodisperse particles (Table 1). Details of the geometry construction, inhalation conditions, and particle transport models are described below.

2.1. Construction of the nasal airway model

The nasal airway is characterized by narrow, convoluted, and multi-layer channels, which create unique aerodynamics. These flow passages help the nose to accomplish its physiological functions. Conversely, reasons for deficient nasal function can often be traced back to abnormal global and local flow conditions and turbulent phenomena in the nasal passages. In an adult, 18,000–20,000 L of air pass through the nose each day. Besides warming and moistening the inhaled ambient air, the nasal cavity also houses olfactory sensory receptors, filters out airborne pollutants, drains excess sinus secretions, and balances pressure between the middle ear and atmosphere.

Table 1
Test conditions for the CS and DF-VC model simulations

Parameter	Range
d_p (nm)	1–1000 nm Ultrafine: 1, 2, 3, 5, 10, 20, 40, 80 Fine: 150, 200, 300, 400, 600, 800, 1000
Inlet flow rate, Q_{in} (L/min)	4, 7.5, 10, 15, 20, 30
Cunningham correction factor, C_c	221–1.15
Particle diffusivity, $\tilde{D}$ (cm^2/s)	5.44×10^{-2} to 2.84×10^{-7}
Schmidt number, Sc	$2.92–5.61 \times 10^{-5}$
Particle Stokes number, St_k	2.4×10^{-8} to 1.0×10^{-3}
Flow Reynolds number at the nasal inlet	189–1413

There are two relatively symmetric passages in the nasal cavity that are separated by the nasal septum (Fig. 1). In each passage, the airway begins with an oval or wedge-shaped nostril which leads to a nearly 90° bend and funnel-like vestibule. The narrow distal end of the vestibule leads to the nasal valve that is the narrowest and most flexible region in the nasal cavity. Collapse of the nasal valve can act as a flow-limiting structure by triggering a switch to combined oral and nasal breathing when inhalation exceeds approximately 34 L/min [44]. Each nasal passage features three curved fin-like airway protrusions known as the superior, middle, and inferior meatus (Fig. 1). The osseous tissues beneath each meatus are termed the superior, middle, and inferior turbinates, respectively, and form the lateral wall of the main passage (Fig. 1). Each turbinate extends nearly the length of the nasal cavity. The two passages merge at the distal end of the nasal cavity and form the beginning of the nasopharynx. The floor of the nasal cavity is formed by the hard palate, which is also the roof the mouth.

To construct the airway model, MRI scan tracings of the nasal cavity for a healthy non-smoking 53-year-old male (weight 73 kg and height 173 cm) were used in this study. The MRI tracings were provided by the Hamner Institutes for Health Sciences (Research Triangle Park, NC) and contained 72 coronal cross-sections spaced 1.5 mm apart spanning the nostrils to the nasopharynx. This geometric dataset was originally reported in the study of Guilmette et al. [45] and has been implemented in a number of nasal particle deposition experiments [46,23,27,24] and simulations [47,13]. The multi-slice tracings were segmented in MIMICS (Materialise, Ann Arbor MI) according to the contrast between osseous structures and intranasal air to convert the raw image data into a set of cross-sectional contours that define the nasal airway. Based on these contours, an internal nasal surface geometry was constructed in Gambit 2.3 (Ansys Inc.) (Fig. 1). The surface geometry was then imported into ANSYS ICEM 10 (Ansys Inc.) as an IGES file for meshing. Due to the high complexity of the model geometry, an unstructured tetrahedral mesh was created with high-resolution pentahedral elements in the near-wall region (Fig. 1b).

Detailed morphometric information including coronal cross-sectional area, perimeter, and hydraulic diameters for the right and left passages are shown in Fig. 2 as a function of distance from the nostril. Comparison of Fig. 2a and b reveals that the dimensions of the two passages are similar but not identical. One difference is the location of the dip in cross-sectional area (i.e., the nasal valve) that occurs at a distance of 25 mm from the nostril in the right passage and 5 mm further downstream in the left. The nasal valve region is marked with an arrow in Fig. 2a and b. In view of the observation that the human nose switches primary inhalation between the left and right nostrils every 90–120 min [48,49], this subtle disparity may be a transient phenomenon.

Another interesting feature of the nasal passages is that even though the available flow area (i.e., coronal cross-sectional area) increases downstream, the effective flow area (which is proportional to the hydraulic diameter) progressively decreases (Fig. 2). This indirect relation results from a consistent increase in the coronal perimeter, which indicates that the nasal airways become increasingly more complex in shape through the nasal passage. This increase in geometric complexity is further illustrated in Fig. 2c in terms of a nasal shape complexity factor, which is defined as the ratio of the hydraulic diameter for a coronal slice and the rectangle bounding that slice. Based on the nasal shape complexity factor, differences are observed between the right and left passages throughout the nasal airway.

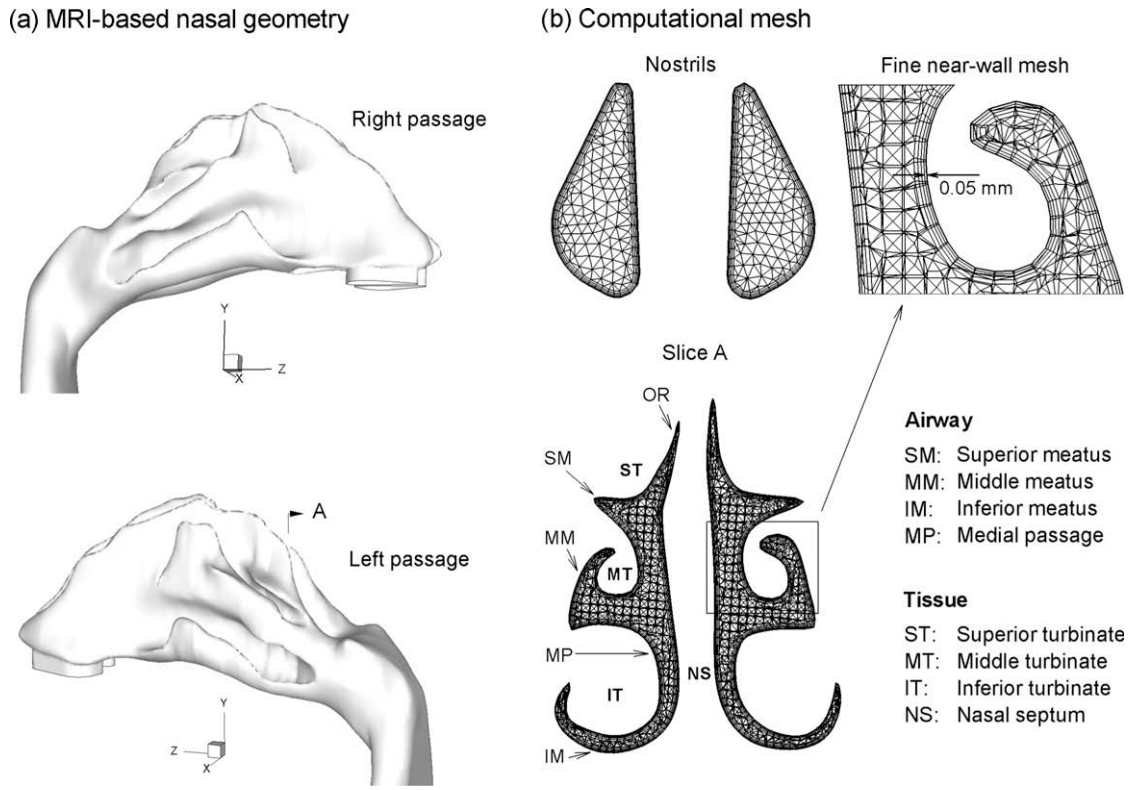

Fig. 1. Computational nasal airway model: (a) realistic surface geometry with asymmetric right and left passages and (b) ICEM-generated computational mesh composed of approximately one million unstructured tetrahedral elements and a very fine near-wall pentahedral grid.

In order to evaluate the performance of the DF-VC model in comparison with the more commonly used CS model on a sub-regional basis, the nasal airway is divided into different sections (Fig. 3). In the horizontal direction, sub-regions include the vestibule, nasal valve region, main passage, and the nasopharynx. The main passage is subdivided vertically into sections including the olfactory region (OR), upper (UP) and lower (LP) passages, the septum wall (SW), and the middle meatus (MM). The upper and lower passages include the superior (SM) and inferior (IM) meatus, respectively. The relative effect of particle inertia on deposition is expected to vary significantly based on the flow heterogeneity within these structures.

2.2. Boundary conditions

Steady inhalation was assumed for all simulations with uniform velocity profiles at both nasal inlets (nostrils) (Fig. 3). The model outlet was extended approximately 20 diameters downstream such that the velocity was normal to the outlet plane (i.e., nearly developed flow profiles with no significant radial velocity component). A constant concentration of the inhaled mass fraction (c_{in}) was assumed for all inhalation rates considered. The nasal surface was assumed smooth and rigid with no-slip ($u_{wall} = 0$) and perfect absorption ($c_{wall} = 0$) conditions. In the body, the nasal cavity is covered with a thin layer of mucus, which captures particles at initial contact and clears them to the vestibule or the back of the throat by mucociliary movement within a time period of 10–15 min. Mass diffusion and metabolism of deposited particles may occur within the mucus layer and may change the zero-concentration conditions at the wall. However, due to the slow speed of the mucociliary movement compared with the intranasal airflow, the no-slip and perfect absorption conditions are reasonable approximations.

2.3. Transport equations

The flow conditions considered in this study are assumed to be isothermal and incompressible. The mean inlet Reynolds number varies from 189 to 1413. The maximum Reynolds number based on the hydraulic diameter of the nasal valve is approximately 8037. The onset of turbulence has been reported to occur at much lower Reynolds numbers in the complex geometries of the respiratory tract in comparison with circular ducts [50]. Therefore, laminar, transitional, and fully turbulent conditions in the nasal cavity are expected. To resolve these multiple flow regimes, the low Reynolds number (LRN) k–ω model was selected based on its ability to accurately predict pressure drop, velocity profiles, and shear stress for transitional and turbulent flows. This model was demonstrated to accurately predict particle deposition profiles for transitional and turbulent flows in models of the oral airway [37,51] and multiple bifurcation units [52]. Moreover, the LRN k–ω model was shown to provide an accurate solution for laminar flow as the turbulent viscosity approaches zero [53].

For laminar and turbulent flow, the Reynolds-averaged equations governing the conservation of mass and momentum are [53]:

$$\frac{\partial u_i}{\partial x_i} = 0 \tag{1}$$

$$\frac{\partial u_i}{\partial t} + u_j \frac{\partial u_i}{\partial x_j} = -\frac{1}{\rho}\frac{\partial p}{\partial x_i} + \frac{\partial}{\partial x_j}\left[(\nu + \nu_T)\left(\frac{\partial u_i}{\partial x_j} + \frac{\partial u_j}{\partial x_i}\right)\right] \tag{2}$$

where u_i is the time-averaged fluid velocity in three coordinate directions, i.e., $i = 1$, 2, and 3, p is the time-averaged pressure, ρ is the fluid density, and ν is the kinematic viscosity. Overbars have not been included on time-averaged quantities to simplify the equations. The turbulent viscosity ν_T is defined as $\nu_T = \alpha^* k/\omega$. For the LRN k–ω approximation, which models turbulence through

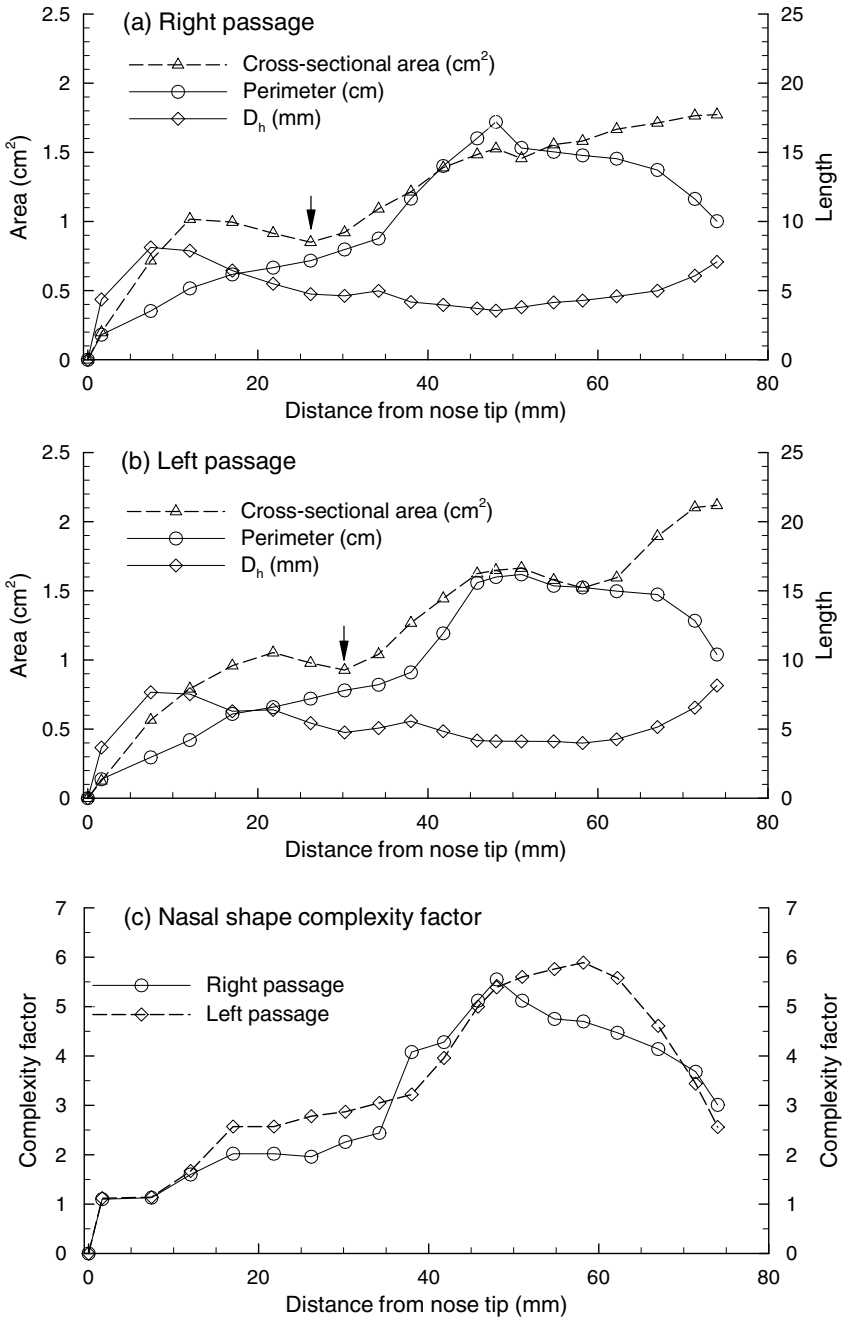

Fig. 2. Nasal airway dimension as a function of the distance from the nose tip in terms of coronal cross-sectional area, perimeter, and hydraulic diameter, D_h, for the (a) right and (b) left passages. The nasal valve is marked with an arrow for the left and right passages. The nasal shape complexity factor is shown in (c), which is defined as the hydraulic diameter ratio of one coronal slice compared with the rectangle bounding that slice.

the viscous sublayer, the α^* parameter in the above expression for turbulent viscosity is evaluated as [53]

$$\alpha^* = \frac{0.024 + k/6v\omega}{1.0 + k/6v\omega} \tag{3}$$

For laminar flow, v_T is zero, and only Eqs. (1) and (2) are solved. Transport equations governing the turbulent kinetic energy (k) and the specific dissipation rate (ω) are provided by Wilcox [53] and were previously reported in Longest and Xi [36].

In this study, two continuous-field particle transport models are evaluated. The first model is the Eulerian chemical species (CS) approximation, which neglects particle inertia [36]. Implementation of this model is intended as a base case to capture convective and molecular diffusive effects. The second model is the drift flux velocity correction (DF-VC) approximation proposed by Longest and Oldham [41].

The transport equation for the CS model governing the convective-diffusive motion of aerosols in the absence of particle inertia can be written on a mass fraction basis as

$$\frac{\partial c}{\partial t} + \frac{\partial (u_j c)}{\partial x_j} = \frac{\partial}{\partial x_j}\left[\left(\tilde{D} + \frac{v_T}{Sc_T}\right)\frac{\partial c}{\partial x_j}\right] \tag{4}$$

In the above equation, c represents the mass fraction of submicrometer particles, $\tilde{D}$ is the molecular or Brownian diffusion coefficient, and Sc_T is the turbulent Schmidt number, which is taken to be 0.9. Assuming dilute concentrations of spherical particles and relatively

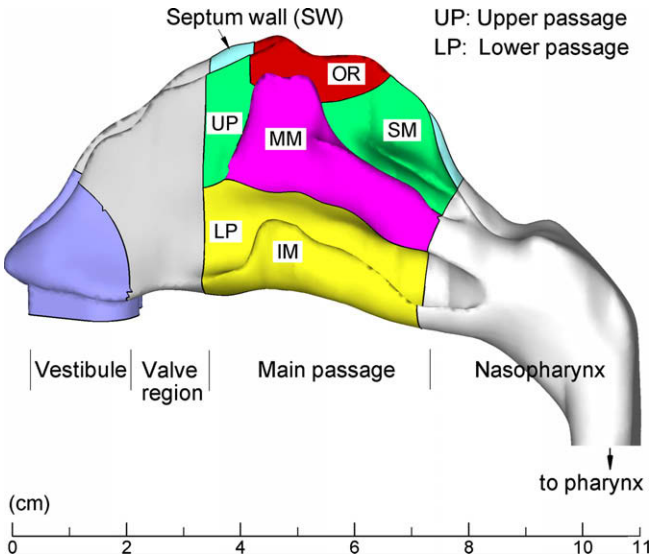

Fig. 3. Division of the nasal airway surface geometry into different anatomical sections to examine sub-regional particle deposition. Sections include the vestibule, nasal valve region, olfactory region (OR), septum wall (SW), middle meatus (MM), as well as the upper (UP) and lower (LP) passages that include the superior (SM) and inferior (IM) meatus, respectively, and the nasopharynx.

long particle time steps compared with molecular collision intervals, the Stokes–Einstein equation is used to determine the diffusion coefficients for various size particles and can be expressed as

$$\widetilde{D} = \frac{k_B T C_c}{3\pi\mu d_p} \tag{5}$$

where $k_B = 1.38 \times 10^{-16}$ cm^2 g/s is the Boltzmann constant in cgs units. The influence of non-continuum effects on the diffusion coefficient and particle drag are accounted for using the Cunningham correction factor [54],

$$C_c = 1 + \frac{\lambda}{d_p}\left(2.34 + 1.05\exp\left(-0.39\frac{d_p}{\lambda}\right)\right) \tag{6}$$

where λ is the mean free path of air. The above expression is reported to be valid for all particle sizes [55]. To approximate particle deposition on the wall, the boundary condition for the Eulerian transport model is assumed to be $c_{wall} = 0$.

For the CS model and laminar or turbulent constant property flow, the local mass deposition rate on a wall is expressed as

$$\dot{m}_{w,l} = -\rho_m A_l\left(\widetilde{D} + \frac{\nu_T}{Sc_T}\right)\frac{\partial c}{\partial n}\bigg|_{wall} \tag{7}$$

where the subscript l indicates local conditions, A_l is the local area, and n is the wall-normal coordinate pointing out of the geometry.

In comparison to the CS model, the most distinct feature of the drift flux approach is the inclusion of the particle velocity (v_j) in the convection transport term, which accounts for particle inertia [41,43]

$$\frac{\partial c}{\partial t} + \frac{\partial (v_j c)}{\partial x_j} = \frac{\partial}{\partial x_j}\left(\left(\widetilde{D} + \frac{\nu_T}{Sc_T}\right)\frac{\partial c}{\partial x_j}\right) \tag{8}$$

In the above equation, the particle velocity (v_j) is evaluated from the particle slip velocity (vs_j),

$$v_j = vs_j + u_j \tag{9}$$

For a continuous-field solution, the particle slip velocity can be determined as a function of inertial and gravity forces as [41,43]

$$vs_j = \frac{C_c d_p^2}{18\mu_c}(\rho_p - \rho_m)\left[g_j - \frac{\partial u_j}{\partial t} - u_i\frac{\partial u_j}{\partial x_i}\right] \tag{10a}$$

where ρ_p and ρ_m are the particle and mixture densities, d_p is the particle diameter, and μ_c is the continuous-field viscosity. In Eq. (10a), the first term in brackets is the gravity vector and the next two terms represent the material derivative, which accounts for fluid element acceleration. For the small particles considered in this study ($\leqslant$1 μm) and high velocity transport in the nasal airways, gravity effects are neglected and particle Stokes flow conditions are assumed. As a result, Eq. (10a) is written in terms of the fluid pressure gradient [41],

$$vs_j = \frac{C_c d_p^2}{18\mu_c}\frac{(\rho_m - \rho_p)}{\rho_m}\frac{\partial p}{\partial x_j} \tag{10b}$$

For the standard drift flux model, slip velocities are only available at control-volume center locations. As a result, the particle velocity at the wall is approximated as the value at the nearest control-volume center. Based on a difference between the particle velocity at the control-volume center and wall surface, Longest and Oldham [41] found that the standard drift flux model over predicted particle inertia and resulted in excessively high particle deposition.

To improve the performance of the standard drift flux approach, Longest and Oldham [41] suggested a velocity correction based on a sub-grid Lagrangian particle solution. The motivation behind this sub-grid solution is that fully resolving near-wall finite particle inertia with a continuous model requires an excessive number of control volumes. Instead, the drift flux velocity correction (DF-VC) model employs an analytic solution of particle velocity between the wall adjacent control-volume center and the wall surface. It is assumed that the continuous-field model correctly approximates particle diffusion within this region, as shown in Longest and Xi [36]. Furthermore, for low particle Reynolds numbers, the individual Lagrangian transport terms become linear and separable. Particle inertia between the control-volume center and wall surface can then be approximated on a discrete Lagrangian basis as [41]

$$\frac{dv_{p,n}}{dt} = \frac{1}{\tau_p}(u_{p,n} - v_{p,n}) \tag{11a}$$

In the above equation, u_p and v_p are the interpolated fluid and particle velocities at the particle location, n is a wall-normal coordinate, and the particle response time is represented as

$$\tau_p = \frac{C_c \rho_p d_p^2}{18\mu_c} \tag{11b}$$

where C_c is the Cunningham correction factor. To formulate an analytic solution of Eq. (11a), the wall-normal *fluid* velocity is assumed to vary linearly between the control-volume center and zero at the wall. The resulting equation for particle position between the wall adjacent control-volume center and the wall surface as a function of time can be written as

$$\frac{d^2 x_p}{dt^2} + \frac{1}{\tau_p}\frac{dx_p}{dt} + \frac{u_{cv,n}}{s\tau_p}x_p = \frac{1}{\tau_p}u_{cv,n} \tag{12}$$

where $u_{cv,n}$ is the fluid velocity at the control-volume center location normal to the wall. An analytic solution to Eq. (12) is possible resulting in wall-normal expressions for particle position [41]

$$x_p(t) = \frac{v_{cv,n} + \lambda_2 s}{\lambda_1 - \lambda_2}e^{\lambda_1 t} - \left(\frac{v_{cv,n} + \lambda_2 s}{\lambda_1 - \lambda_2} + s\right)e^{\lambda_2 t} + s \tag{13a}$$

and velocity

$$v_{p,n}(t) = \frac{v_{cv,n} + \lambda_2 s}{\lambda_1 - \lambda_2}\lambda_1 e^{\lambda_1 t} - \left(\frac{v_{cv,n} + \lambda_2 s}{\lambda_1 - \lambda_2} + s\right)\lambda_2 e^{\lambda_2 t} \tag{13b}$$

where

$$\lambda_1 = \frac{1}{2}\left(-\frac{1}{\tau_p} + \sqrt{\left(\frac{1}{\tau_p}\right)^2 - 4\left(\frac{u_{cv,n}}{s\tau_p}\right)}\right) \quad \text{and}$$

$$\lambda_2 = \frac{1}{2}\left(-\frac{1}{\tau_p} - \sqrt{\left(\frac{1}{\tau_p}\right)^2 - 4\left(\frac{u_{cv,n}}{s\tau_p}\right)}\right) \tag{13c\&d}$$

The time for initial wall contact can be determined from Eq. (13a). The associated particle velocity at the point of deposition is then calculated using Eq. (13b).

As with the CS model, the drift flux approach assumes perfect absorption at the wall, i.e., $c_{wall} = 0$. The associated local mass deposition as a result of both diffusional and inertial effects is expressed as

$$\dot{m}_{w,l} = -\rho_m A_l \left(\widetilde{D} + \frac{\nu_T}{Sc_T}\right)\frac{\partial c}{\partial n}\bigg|_{wall} + \rho_m A_l c v_n|_{wall} \tag{14a}$$

In the above expression, v_n represents the wall-normal particle velocity scalar

$$v_n = v_i \hat{n}_i \tag{14b}$$

where $\hat{n}_i$ is the local wall-normal unit vector pointing out the geometry. In a standard drift flux model, the value of v_n is not available at the wall. As a result, it is typically approximated as the value at the nearest control-volume center. In contrast, the DF-VC approach calculates the approximate particle velocity at the wall ($v_n|_{wall}$) using Eq. (13b). This value is then implemented in Eq. (14a) to compute the local mass deposition rate.

2.4. Deposition factors

The local deposition fraction in a designated nasal region is defined as the ratio of particles depositing within that region to the particles entering the nostrils. For the continuous-field models considered in this study, the local deposition fraction (Df_l) is based on the ratio of the local mass deposition rate to the inlet mass flow rate over time

$$Df_l = \frac{\dot{m}_{w,l}}{\dot{m}_{in}} \tag{15a}$$

where the local wall mass flow rates $\dot{m}_{w,l}$ for the CS and DF-VC models are available from Eqs. (7) and (14), respectively. The total inlet mass flow rate of particles is calculated as

$$\dot{m}_{in} = 2\rho_m c_{in} u_{in} A_{nostril} \tag{15b}$$

In the above expression, c_{in} is the constant inlet mass fraction of particles, $A_{nostril}$ is the area of one nostril, and the factor 2 is used to account for equal inhalation through both nostrils. The total or regional deposition fraction within the nasal geometry is calculated as

$$Df = \frac{\sum_{l=1}^{N}\dot{m}_{w,l}}{\dot{m}_{in}} = \sum_{l=1}^{N} Df_l \tag{16}$$

where the summation is performed over the N local areas of interest.

In order to capture local deposition profiles for the Eulerian model, a deposition enhancement factor (DEF), similar to the enhancement factor suggested by Balashazy et al. [56], for local region l can be defined as

$$DEF = \frac{Df_l/A_l}{\sum_{l=1}^{N} Df_l / \sum_{l=1}^{N} A_l} = \frac{Df_l/A_l}{Df_r/A_r} \tag{17}$$

where the summation is performed over the region of interest. In this study, the local area of interest A_l for evaluating DEF is considered to be wall-adjacent surfaces of control volumes and the region of interest is the entire nasal surface geometry. Therefore, A_l represents a variable control volume surface area as was implemented in other studies [39]. The numerator of the DEF term is proportional to the local mass flux, which represents a point-value in a variable surface field. Provided that a sufficiently fine grid is used to resolve this surface field, mass flux values should be independent of the sampling area A_l selected and DEF values can be considered area-independent. Physically, the DEF parameter represents the local proportion of deposition relative to the mean value for the region considered. That is, a DEF value of 10 indicates that the local fraction of deposition (Df_l) for region A_l is 10 times higher than the area-averaged mean deposition fraction (Df) for the entire region.

For inhaled aerosols, the mass flux $\dot{n}$ depositing on the wall is driven by the concentration gradient between the air stream and surface, Δc

$$\dot{n} = K_C \cdot \Delta c = K_C \cdot [c_B(x) - c_{wall}] \tag{18}$$

Here, K_C is the respiratory mass transfer coefficient and $c_B(x)$ is the bulk concentration over the airway cross-section normal to the axial direction at location x. Unlike gases or vapors, respiratory particles typically adhere once contact is made with the wall, which is approximated by applying $c_{wall} = 0$. As a result, the local mass flux can be calculated based on the particle depletion from the gas phase for a given axial length dx,

$$\dot{n} \cdot P(x) \cdot dx = -Q\, dc_B(x) \tag{19}$$

where $P(x)$ is the perimeter of the airway cross-section at x and Q is the volumetric flow rate. After rearrangement of Eqs. (18) and (19) and integration, K_C can be expressed as

$$K_C = -\frac{Q}{A_s} \cdot \ln\left(\frac{c_{B,out}}{c_{B,in}}\right) \tag{20}$$

where $c_{B,out}$ and $c_{B,in}$ are the outlet and inlet bulk concentrations, respectively, and A_s is the surrounding wall surface area available for deposition. The Sherwood number is a dimensionless group based on the ratio of convective mass transport to molecular diffusivity between the wall and bulk fluid, i.e.,

$$Sh = \frac{K_C \cdot D_h}{\widetilde{D}} \tag{21}$$

The hydraulic diameter of a single nostril (D_h) has been employed for the calculation of the Sherwood and inlet Reynolds (Re) numbers.

2.5. Numerical method and convergence sensitivity analysis

To solve the governing mass and momentum conservation equations in each of the cases considered, the CFD package Fluent 6 was employed. User-supplied Fortran and C programs were implemented for the calculation of initial particle profiles, particle deposition factors, grid convergence, and deposition enhancement factors. For this study, a specific set of user-defined functions was developed for implementation of the CS and DF-VC models. User modules were written for the calculation of slip velocities, particle velocity at the wall, the mass fraction advection term, and mass deposition. All transport equations were discretized to be at least second order accurate in space. A segregated implicit solver was employed to evaluate the resulting linear system of equations. This solver uses the Gauss–Seidel method in conjunction with an algebraic multi-grid approach for improving the calculation performance on tetrahedral meshes. The SIMPLEC algorithm was employed to evaluate pressure–velocity coupling. Convergence of the flow field solution was assumed when the global mass residual was reduced from its original value by five orders of magnitude and when the residual-reduction-rates for both mass and

momentum were sufficiently small. To ensure that a converged solution was reached, residual and reduction-rate factors were decreased by an order of magnitude and the results were compared. The stricter convergence criteria produced a negligible effect on both velocity and particle deposition fields.

To accurately capture the turbulent–particle interactions, it is necessary to model the turbulence down to a near-wall y^+ value of 1. Accordingly, a grid convergence study of the particle transport models was considered. Grids consisting of 56,800, 740,100, 1,055,200, and 1,711,000 control volumes were evaluated. Each successive grid refinement reduced the near-wall control volume height by a factor of 2. Increasing grid resolution from 1,055,200 to 1,711,000 control volumes resulted in total deposition changes less than 1% for both the DF-VC and CS models. As a result, the final grid for reporting flow field and deposition conditions consisted of approximately 1,055,200 cells with a thin five-layer pentahedral grid in the near-wall region (Fig. 1b). The height of first near-wall cell was 0.05 mm, resulting in wall y^+ values of approximately $y^+ = 1$ for all inhalation flow rates considered in this study.

3. Results

3.1. Flow fields

Steady state flow fields in the nasal airway for an inhalation flow rate of 20 L/min are shown in Fig. 4. In the three-dimensional field (Fig. 4a) and partial sagittal view (Fig. 4b), flows of high velocity magnitude are observed in the middle portion of the medial passage. The extreme curvature of the core flow is apparent, forming an 180° bend from the nostril inlet through the nasopharynx. A recirculation zone is observed in the upper part of the nasopharynx as a result of expansion in both cross-sectional and effective (i.e., hydraulic) flow areas. The narrow meatus regions receive a minimal fraction of the airflow, especially in the peripheral portions of each meatus. However, careful examination of the coronal view in Fig. 4c reveals some discernable differences among the three meatus regions that are associated with the unique nasal airway structure. In the anterior nasal passage (Slice 2–2′), the flow progresses further in the inferior meatus than in the middle meatus. This preference results from the fact that more air enters through the base of the triangular-shaped nostrils. After changing direction by approximately 90° in the nasal vestibule and valve regions, an elevated portion of flow enters the lower nasal airway that includes the inferior meatus. In the downstream slices (i.e., Slices 3–3′ and 4–4′), flow is observed to spread upward toward the upper passage near the middle turbinate, partly due to the main streamline curvatures.

To illustrate the effect of secondary velocity motion, two-dimensional stream traces are shown in selected portions of two coronal slices (Slices 1–1′ and 3–3′). Due to the thin air channels, vortices are damped in the nasal passages. However, a vortex is observed near the floor of the valve region, as illustrated in Fig. 4c. The magnitude of the secondary velocity in each slice is approximately 30% of the main flow. This secondary velocity component functions to distribute the inhaled air into each fin-like meatus. Of particular interest is the observation that these secondary veloc-

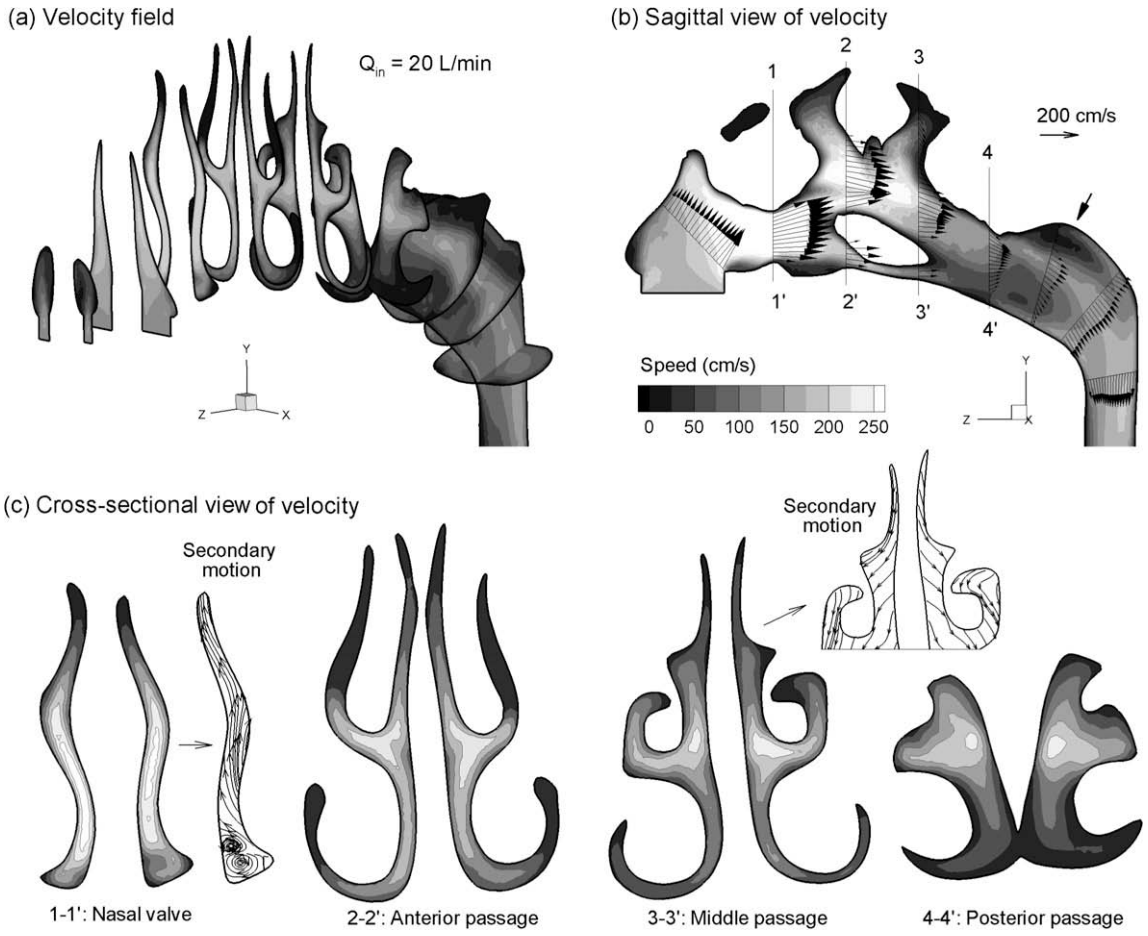

Fig. 4. Velocity fields in the nasal passages at an inhalation flow rate of 20 L/min in (a) 3-D, (b) sagittal, and (c) cross-sectional (coronal) views. The filled arrow marks the location of flow separation and recirculation in the nasopharynx.

ities also distribute flow toward the olfactory region. As air progresses in and out of the projecting airways, the resulting secondary streams move upward prior to the olfactory region (Slice 1-1′) and downward after the olfactory region (Slice 3-3′). It is expected that this secondary motion near the olfactory region is delicately balanced in order to convey a sufficient amount of particles or vapors for the olfactory nerve to perceive while remaining small enough to protect this extremely sensitive area that is directly connected to the brain.

The evaluation of turbulence in the nasal airway is shown as Fig. 5 in terms of turbulent kinetic energy, k, and more practically, the turbulent viscosity ratio, ζ, which is the ratio of total to laminar viscosity $\zeta = (\nu_T + \nu)/\nu$. In this expression, ν and ν_T are the laminar and turbulent kinematic viscosities, respectively. From Fig. 5a and b, turbulence is noted mainly in the nasal vestibule and valve regions, and at a lower intensity in the dorsal region of the nasopharynx. Relatively weak turbulence is observed in the nasal main passage. In contrast, significant turbulence occurs in the nasal valve region, which is coincident with the peak wall shear stress. The turbulence characteristics are further illustrated as iso-surfaces of constant magnitude in Fig. 5c–e. Fig. 5d shows the iso-surface of $\zeta = 2$, which implies equivalent laminar and eddy viscosities. This contour level is observed in the vestibule, valve region, the anterior portion of the inferior turbinate, nasopharynx, and downstream pharynx. Only two attenuated strips are observed through the main nasal passage, suggesting that the major portion of this complex region can be regarded as laminar. Fig. 2e displays conditions for which the turbulent viscosity is one order of magnitude above the laminar viscosity ($\zeta = 10$). In this scenario, enhanced viscosity is limited primarily to the anterior vestibule and a small region of the dorsal nasopharynx, where either severely curved flow or flow reversal occurs.

3.2. Particle transport

Fig. 6 displays the mass concentration profiles in the nasal passage for 400 nm monodisperse particles at an inhalation flow rate of 20 L/min. Overall, the concentration distributions bear a strong resemblance with the velocity field depicted in Fig. 4, indicating that submicrometer particles are closely following the main flow. The particle concentration profiles are attenuated along the mainstream direction as a result of increasing flow areas, enhanced mixing from turbulence, and particle depletion due to wall depositions. In the coronal view of the anterior passage shown in Slice 2–2′ (Fig. 6c), low particle concentrations are observed inside the middle meatus due to the steep transition from the nasal valve to this fin-like narrow structure. Beyond the anterior passage (Slice 2–2′), the fin-like middle meatus tapers in size in a relatively smooth manner until it merges with the nasopharynx. As a result, secondary flows drive particles into deeper regions of the middle meatus at Slice 3–3′ (Fig. 6c). With regard to the olfactory region, only a small portion of particles is observed to approach this area.

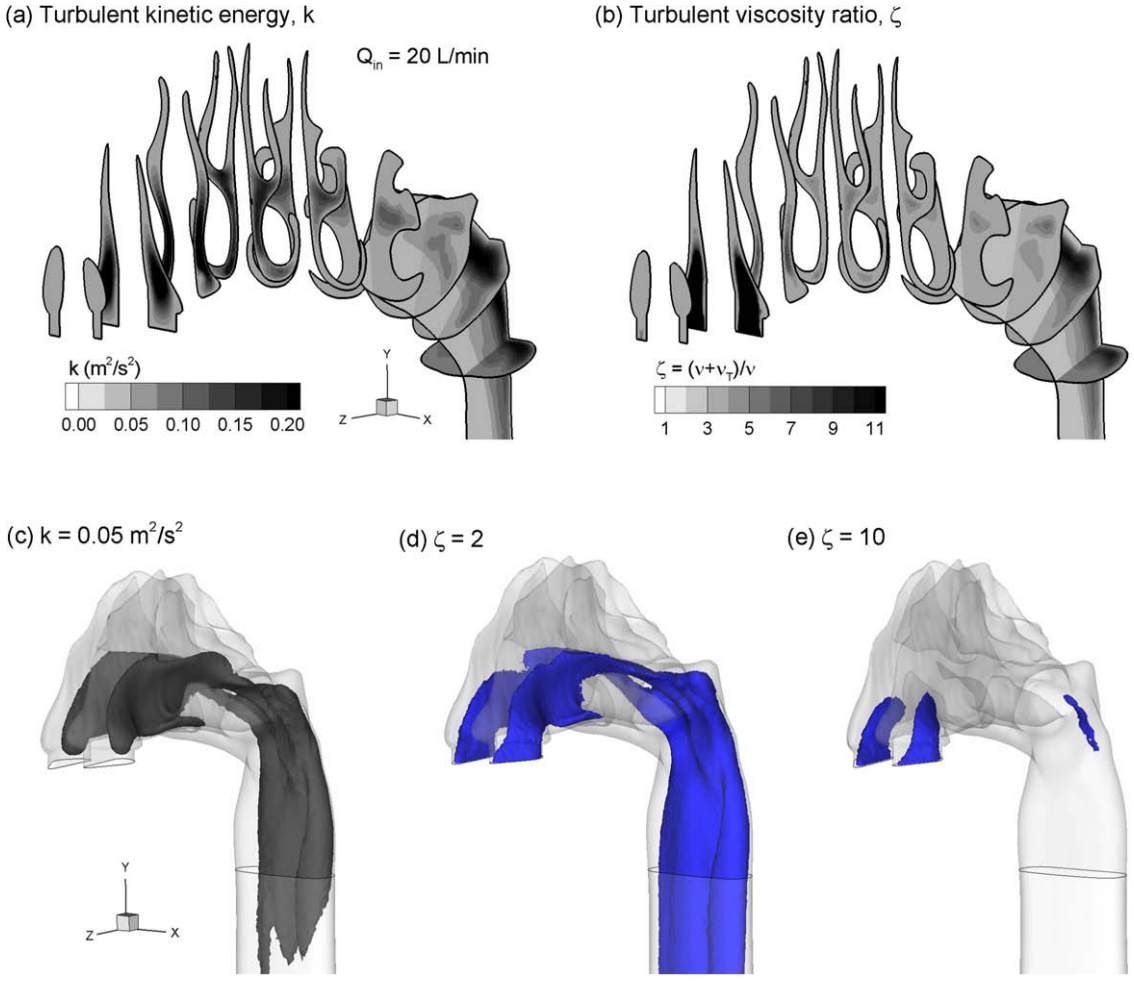

Fig. 5. Turbulence quantities in the nasal passages at an inhalation flow rate of 20 L/min: (a) turbulent kinetic energy, k and (b) effective viscosity ratio, $\zeta = (\nu + \nu_T)/\nu$. Iso-surfaces of turbulence parameters are illustrated for (c) $k = 0.05$ m^2/s^2, (d) $\zeta = 2$, and (e) $\zeta = 10$.

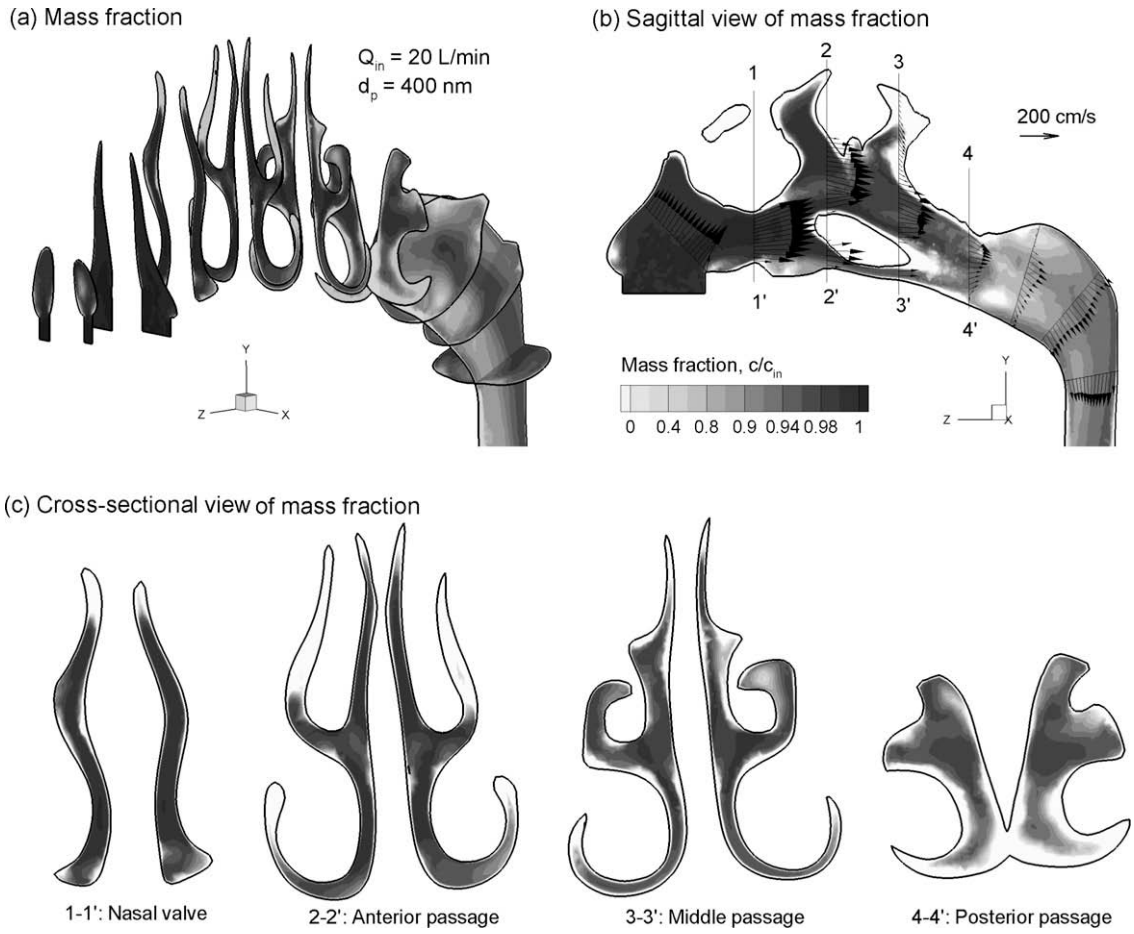

Fig. 6. Normalized mass fraction contours (c/c_{in}) of 400 nm particles in the nasal passages at an inhalation flow rate of 20 L/min in (a) 3-D, (b) sagittal, and (c) cross-sectional views.

3.3. Particle deposition

Fig. 7a and b show comparisons of particle deposition fractions between the novel DF-VC model and *in vitro* experiments in various nasal replicas for inhalation flow rates of 10 and 20 L/min, respectively. A summary of test conditions for the displayed experimental results is listed in Table 2. In the table, SLA and Viper refer to nasal models constructed with different rapid prototyper machines. Considering that the computational geometry of this study and the nasal replica SLA, Viper, and ANOT2 (adult-nasal–oral–tracheal) geometries were all constructed based on the same set of nasal images, a direct comparison of deposition data is possible. It is observed in Fig. 7 that despite the highly scattered nature of the experimental data, reasonable agreement between the DF-VC simulation and *in vitro* measurements is obtained for both of the flow rates considered. For an inhalation flow rate of 10 L/min, the simulation results agree with the ANOT1 and ANOT2 [46] data to a high degree, and appear to be 5–10% lower than the SLA and Viper data sets reported by Kelly [24] across the range of particle sizes considered (Fig. 7a).

For an inhalation flow rate of 20 L/min, the DF-VC model predictions are in general agreement with the lower boundary of the *in vitro* results, as with the ANOT1 and ANOT2 geometries, across a range of submicrometer aerosols (Fig. 7b). However, the CFD estimates appear to under predict the mean values considering the experimental data set as a whole. Comparing experimental deposition results for inhalation flow rates of 10 (Fig. 7a) and 20 (Fig. 7b) L/min, it is interesting to note that the total mean deposition fraction remains relatively invariant for each particle size. For example, the mean *in vitro* nasal deposition for 5 nm particles is approximately 25% at both 10 and 20 L/min. In contrast, the DF-VC model does predict differences in deposition between the two flow rates considered. For 5 nm particles, predicted deposition rates at 10 and 20 L/min are 15% and 10%, respectively. The deposition of 5 nm particles in the nasal cavity is expected to be controlled primarily by Brownian diffusion and, to a lesser extent, by convective diffusion. Therefore, it would appear more likely that the deposition of 5 nm particles should decrease as the flow rate is doubled. Considering this observation, it appears that a significant amount of variability is present in the experimental data, even though three of the *in vitro* nasal models originated from a similar data set. Factors that may contribute to this variability and the related underestimation of deposition by the numerical model may include minor geometry differences and electrostatic effects. Nasal deposition is highly sensitive to airway dimensions; however, even based on the same data set, different preparation methods may result in geometrical discrepancies of varying degrees (Table 2). Moreover, depositions for charged submicrometer particles, even at the Boltzmann equilibrium, could be several times that of charge-free particles [57]. Charge-neutralization of aerosols in replica experiments can minimize the electrostatic effect; however, some charge remains on the charge-neutral particles. Despite these underestimations, the DF-VC simulation agrees reasonably well with measurements in the four experiments that were considered.

To further evaluate predictions of the DF-VC model, nasal deposition fractions from Fig. 7 are plotted as a function of different

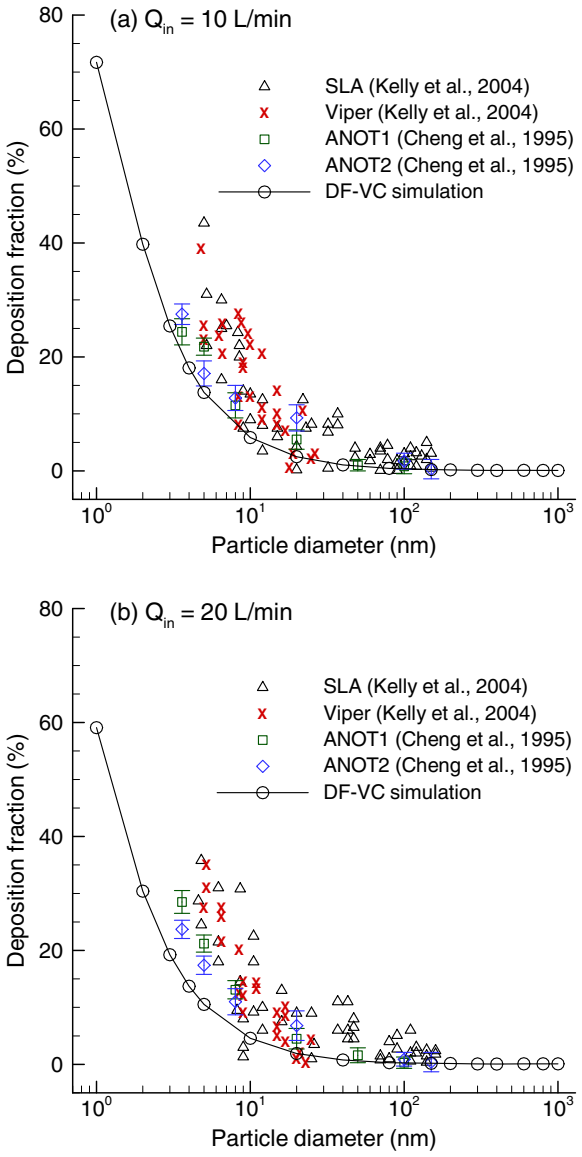

Fig. 7. Comparison of particle deposition fractions as a function of particle diameter between DF-VC simulations and *in vitro* experiments at an inhalation flow rate of (a) 10 L/min and (b) 20 L/min.

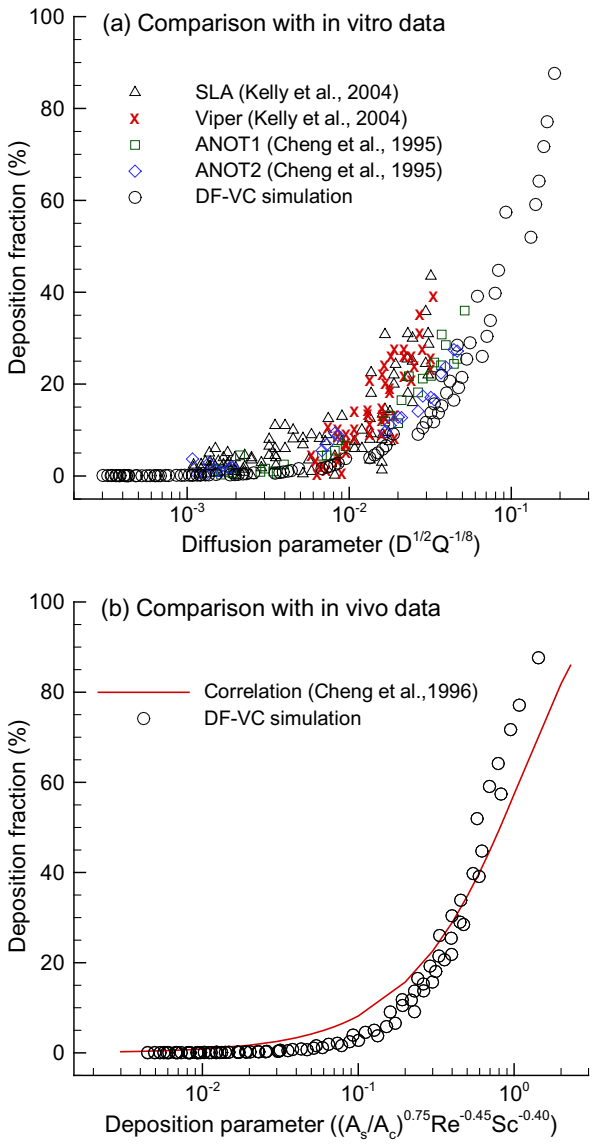

Fig. 8. Comparison of DF-VC predicted deposition fractions as a function of grouped diffusion parameters with (a) *in vitro* measurements and (b) an *in vivo*-based correlation for particles ranging from 1 to 1000 nm and inhalation flow rates ranging from 4 to 30 L/min.

deposition parameters which have been suggested by other studies (Fig. 8). Inhalation flow rates that were considered in Fig. 8 included 4, 7.5, 10, 15, 20, and 30 L/min with particle sizes ranging from 1 to 1000 nm. Fig. 8a shows a comparison of the deposition fractions for the DF-VC simulation and replica measurement as a function of a diffusion parameter suggested by Cheng et al. [46]. Again, good agreement exists between the simulations and measurements for the four replica casts that were considered. Specifically, the closely correlated association of deposition fraction with the parameter $(\widetilde{D}^{1/2}Q^{-1/8})$ indicates a stronger dependence of nasal deposition on particle diffusivity (exponent of 1/2) than on flow rate (exponent $-1/8$) for the submicrometer particles considered. The same data reported in Fig. 8a are plotted versus a deposition parameter $[(A_s/\overline{A_c})^{0.75}Re^{-0.45}Sc^{-0.40}]$ in Fig. 8b and compares favorably with an empirical correlation based on *in vivo* nasal depositions proposed by Cheng et al. [26]. In this parameter, A_s is the nasal surface area and $\overline{A_c}$ is the average cross-sectional area of the nasal passage.

Table 2
Summary of nasal *in vitro* experiments

Replica	Geometry	Original data source	Method	A_c (cm^2)	Particle size (nm)
SLA [24,27]	Nostrils to posterior pharynx	MRI images of 53-year-old male	Rapid prototyping 0.05 mm resolution	~3.10	5–150
Viper [24,27]	Nostrils to posterior pharynx	MRI images of 53-year-old male	Rapid prototyping 0.10 mm resolution	~3.10	5–150
ANOT1 [46]	Nostrils to upper trachea	Cadaver specimen	Wax casting	5.56	3.6–100
ANOT2 [46]	Nostrils to upper trachea	Nasal cavity: MRI of 53-year-old male; laryngeal–tracheal cadaver specimen	Wax casting	4.80	3.6–150

3.4. Mass transfer correlations

Fig. 9 shows the Sherwood number (*Sh*) in the nasal airway geometry as a function of the Stokes number (St_k) determined using the DF-VC model compared with the standard chemical species (CS) model. As described previously, the DF-VC approximation accounts for both particle inertia and diffusion, whereas the CS model only considers particle diffusion. As a result, the increased deposition of the DF-VC model compared with the CS approach can be attributed entirely to particle inertia. For ultrafine particles where inertial effects are negligible, the Sherwood number *Sh* is nearly identical for the two models considered. Deviation of *Sh* between the DF-VC and CS models begins at $St_k = 1.0 \times 10^{-5}$ and becomes progressively significant with increasing St_k. Accordingly, a critical value above which inertia significantly influences deposition is identified as $St_k = 1.0 \times 10^{-5}$. Compared with the inertia limit of $St_k = 5.0 \times 10^{-5}$ for tracheobronchial airways [36], this smaller value in the nasal cavity indicates an earlier onset of particle inertia effects, which may be due to the high complexity of this geometry. It is interesting to note that the Sherwood number has a significant and direct relationship with the Stokes number even in the diffusional region, implying a strong association between mass transfer and St_k for ultrafine particles. This is not surprising considering the fact that the Stokes number is related to particle size and, therefore, an inverse indicator of particle diffusivity.

While the nasal deposition can be reasonably predicted by existing empirical correlations, these expressions are typically limited to ultrafine and coarse particles where either inertial impaction or diffusion are the predominate mechanisms for particle loss. In contrast, a correlation is sought in this study that is valid for both inertial and diffusional deposition mechanisms and can be applied for all submicrometer particles. Fig. 10 shows the development of a mass transfer correlation in the nasal cavity in terms of the non-dimensional Sherwood number. The dependence of mass transfer on convective diffusion is plotted in Fig. 10a with a best-fit correlation for the diffusion zone as

$$Sh = (Re^{0.55}Sc^{0.60})^{0.553} = Re^{0.30}Sc^{0.33} \quad (Re^{0.55}Sc^{0.60} \leqslant 1.5 \times 10^4 \text{ or } St_k \leqslant 1.0 \times 10^{-5}) \tag{22}$$

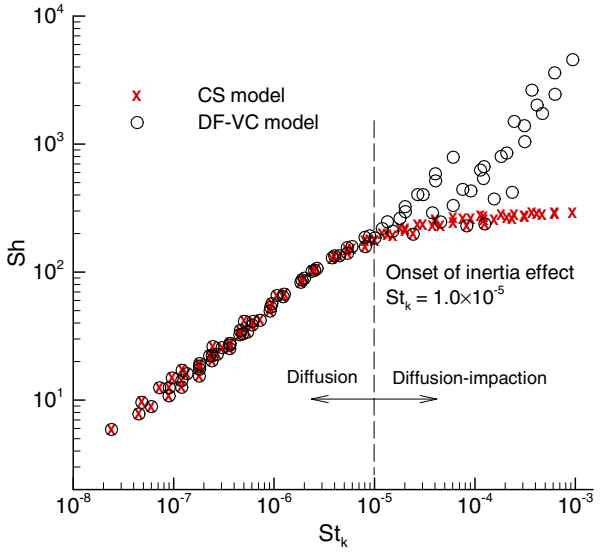

Fig. 9. Comparison of a numerically determined Sherwood number, *Sh*, as a function of Stokes number, St_k, between the CS and DF-VC models. Deviation of *Sh* between these two models occurs at $St_k = 1.0 \times 10^{-5}$ and indicates the onset of particle inertia and impaction.

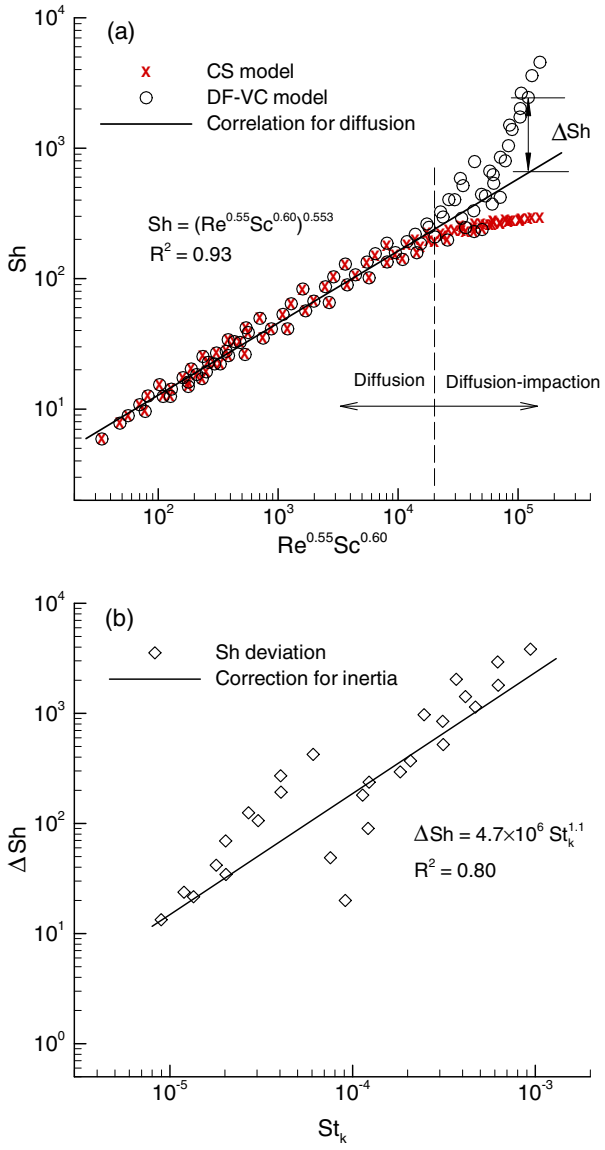

Fig. 10. Development of a Sherwood number *Sh* correlation in the nasal airway that accounts for both diffusional and inertial deposition mechanisms for submicrometer aerosols: (a) correlation for ultrafine particles where diffusion dominates deposition and (b) correlation for enhanced mass transport due to particle inertia, ΔSh, as a function of Stokes number, St_k.

The convective-diffusion coefficient ($Re^{0.55}Sc^{0.60}$) adopted here was suggested by Cheng et al. [26] for *in vivo* nasal deposition data, which is similar to the deposition parameter in Fig. 8b. For fine respiratory particles that are influenced by diffusion and impaction deposition mechanisms, the deviation from the above equation (ΔSh, see Fig. 10a) due to particle inertia can be correlated as a function of St_k using (Fig. 10b)

$$\Delta Sh = 4.7 \times 10^6 St_k^{1.1} \quad (St_k \leqslant 1.0 \times 10^{-3}) \tag{23}$$

Based on the assumption of weak coupling between the inertial and diffusive deposition mechanisms, the overall correlation that is valid for all submicrometer particle sizes can be obtained by adding Eqs. (22) and (23) as

$$Sh = Re^{0.30}Sc^{0.33} + 4.7 \times 10^6 St_k^{1.1} \quad (St_k \leqslant 1.0 \times 10^{-3} \text{ or } d_p = 1\text{–}1000\ \text{nm}) \tag{24}$$

Alternatively, the above correlation can be expressed in terms of total nasal deposition fraction,

$$\mathrm{Df} = 1 - \exp\left[-\left(\frac{A_s}{\overline{A_c}}\right)\left(Re^{-0.70}Sc^{-0.67} + 4.7\times 10^{6}\frac{St_k^{1.1}}{ReSc}\right)\right] \quad (d_p = 1\text{—}1000\ \mathrm{nm}) \tag{25}$$

where A_s is the total surface area and $\overline{A_c}$ is the mean cross-sectional area of the nasal passage.

3.5. Local and sub-regional deposition results

To highlight the effect of finite particle inertia on deposition localization, a comparison of deposition enhancement factors (DEF) predicted using the CS and DF-VC models is shown in Fig. 11 for 400 nm particles at an inhalation flow rate of 30 L/min. With DEF values plotted on the same scale, the difference between these two models is striking. In contrast to the more uniformly distributed DEF values of the CS model, the deposition with the DF-VC model is significantly more heterogeneous and localized. Specifically, at the anterior junction point (solid circle) between the middle meatus (MM) and medial passage (MP) where high-speed flow and steep geometry transition occur, the hot spot of the DEF value predicted by the DF-VC model is about five times higher than the CS value. Another expected hot spot is at the superior part of the vestibule (dashed square), which is captured by the DF-VC model. In contrast, the CS model does not indicate this region as having elevated deposition. Additionally, elevated deposition accumulations are also predicted around the rear olfactory region (filled arrow) based on the DF-VC model due to particle trajectory deviations from curved streamlines in the main airflow. These elevated localizations may have important implications in chemical sensing applications or nasal drug delivery for neurological disorders where the olfactory region is the targeted deposition site.

The effectiveness of the DF-VC model in capturing inertial and diffusive deposition is further illustrated in Fig. 12 in terms of deposition within specific sections of the nose. The extent of each section is depicted in Fig. 3 and the inhalation conditions are identical to those shown in Fig. 11 (i.e., Q_{in} = 30 L/min and 400 nm particles). The magnitude of the deposition fraction value for each region (except for the nasopharynx) represents the summation of right (lower bar) and left (upper bar) nasal passages. The deposition fraction values for the CS model denote deposition from diffusion only, while the difference between the DF-VC and CS models can be viewed as deposition from inertial impaction. In

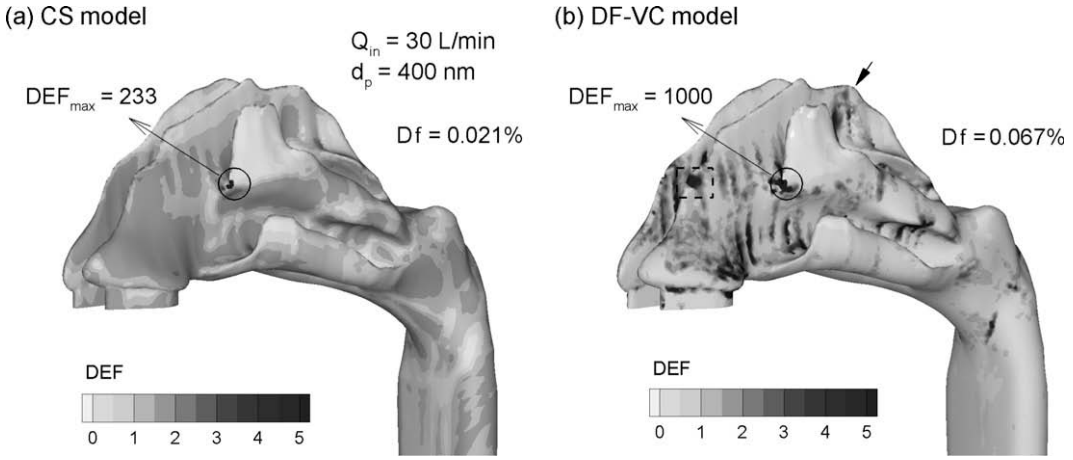

Fig. 11. Numerically determined deposition enhancement factors (DEF) in the nasal airway for 400 nm particles at an inhalation flow rate of 30 L/min using the (a) CS and (b) DF-VC models.

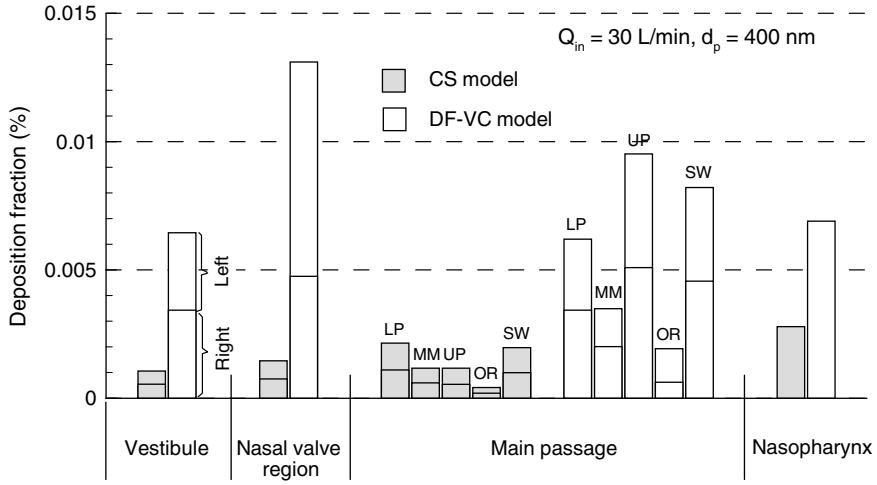

Fig. 12. Comparison of deposition fractions between the CS and DF-VC models in different nasal sections. The magnitude of the deposition fraction values in the anterior and main nasal airway is the summation of the right (lower bar) and left (upper bar) nasal passages.

the vestibule, where the direction of airflow changes by approximately 90°, significantly enhanced deposition is predicted by the DF-VC model, which is about 6.1 times the CS model estimate for identical conditions. An even more pronounced effect of inertial impaction (i.e., an order of magnitude increase) is found in the nasal valve region where the cross-sectional area is minimal and the airflow passages are narrowest. In this region, the valve-associated stenosis, flow acceleration, and short distances to the walls combine to effectively increase the inertial deposition of particles entrained in the flow. The inertial effect on deposition in the main passage remains significant, but to a lesser degree in comparison with the vestibule and nasal valve regions, which is likely due to the increased flow area (decreased flow speed) and less severe streamline curvatures (Fig. 12). Within the main passage, diffusion is enhanced in the middle and inferior meatus by the slow-moving flows (and the resulting prolonged particle residence times) as well as the large surface areas of these two fin-like projections available for particle contact. As a result, the deposition fraction of the DF-VC model is only 3.0 times that of the CS model for the middle meatus (MM) and 2.9 times larger for the lower passage (LP).

4. Discussion

To improve the simulation of submicrometer aerosols in the respiratory tract, a novel continuous-field drift flux model (i.e., DF-VC) was previously developed by Longest and Oldham [41], which includes finite particle inertia and a sub-grid near-wall velocity correction. In this study, the DF-VC model was shown to provide a good match to experimental *in vitro* measurements and an existing *in vivo* empirical correlation for submicrometer particle deposition in the human nasal airways. Moreover, the DF-VC model appears to capture the effects of particle inertia that become significant relative to diffusion for fine (100–1000 nm) respiratory aerosols. Accurate predictions of deposition arising from both impaction and diffusion for submicrometer aerosols are very important considering the health effects associated with exposure to cigarette smoke (140–500 nm) and diesel exhaust (50–500 nm) particulate matter. Another appealing aspect of the DF-VC model is its high computational efficiency in comparison with the commonly used Lagrangian particle tracking approach, which requires a tremendous number of submicrometer discrete particles to obtain fully converged deposition solutions. For example, considering 400 nm particles, the Lagrangian approach requires approximately 1×10^6 and 1×10^7 particles to obtain converged total and local deposition values, respectively, which is equivalent to about 10 and 100 h of additional computational time on a current single processor machine. In contrast, solution of the drift flux model considered in this study requires approximately 0.2 h of additional computational time and provides converged regional and local deposition results. Therefore, the drift flux (DF-VC) model decreased simulation times by 2–4 orders of magnitude in comparison with a standard Lagrangian tracking approach.

While the DF-VC model has been shown to be highly effective, it does have several limitations. The current DF-VC model was developed mainly for fine respiratory aerosols based on the use of the pressure gradient term in Eq. (10b). This model can also be extended to larger particle sizes if Eq. (10a) is used to compute the particle slip. Another limitation of the general drift flux approach is the assumption of a dilute aerosol in which the momentum of the discrete phase does not influence the flow field. As a result, low loadings of particle concentration are required, which is generally the case for respiratory aerosols. Finally, the current model was developed for monodisperse aerosol distributions.

Factors that limit the physical realism of the current study include the assumptions of steady flow, simplified inlet conditions, a smooth and rigid airway surface, a constant nasal valve aperture for various breathing conditions, and a model from a single subject. Other studies have highlighted the physical significance of transient breathing [13], inlet velocity profiles [58,59], nasal wall motion [60], and nasal valve change during respiratory maneuvers [61,62]. Moreover, the nasal model in this study is based on images of a single subject acquired at the end of expiration and, therefore, does not account for intersubject [63,64] or intrasubject [48,49] variability. Each of these factors influences the realism of the model predictions in relation to actual particle deposition in the nose. However, a primary objective of this study was to assess the performance of a newly developed two-phase transport model for simulating fine respiratory aerosols in nasal airways. Achieving this objective was facilitated by the geometry and flow condition assumptions that were made.

In conclusion, the total and local depositions of submicrometer aerosols in the nasal cavity were assessed using a novel drift flux transport model that accounts for particle diffusion and inertia. Performance of the DF-VC model was evaluated in a realistic nasal model through comparisons with *in vivo* and *in vitro* deposition data and correlations. Simulation results of the DF-VC model were also compared to that of a standard chemical species (CS) model, which neglects the particle inertia force, to highlight the effects of particle inertia on the deposition of fine and ultrafine respiratory aerosols. Simulations were conducted for a variety of scenarios that covered inhalation flow rates from 4 to 30 L/min and particle sizes ranging from 1 to 1000 nm. For the first time, the inertial effects of fine particles on deposition relative to diffusional effects were evaluated in the nasal airway for laminar through turbulent flow regimes. Differences in submicrometer particle deposition with and without inertia were evaluated on a regional, sub-regional, and localized basis. Specific findings of this study include:

1. Airflow in the nasal cavity was mostly laminar and transitional under moderate breathing conditions (Q_{in} = 20 L/min), with turbulence occurring mainly in the nasal vestibule-valve region and dorsal nasopharynx (Fig. 5). Laminar flow was dominate in the main nasal passage.
2. Reasonable agreement of the total nasal deposition fraction was obtained between the DF-VC model predictions and experimental measurements in similar nasal replicas. The model predictions corroborated an existing empirical correlation of *in vivo* nasal deposition [26] for ultrafine particles (Fig. 8).
3. Finite particle inertia was found to play a significant role in the total deposition of fine respiratory aerosols in the nasal airway and has an even more pronounced impact on the localized deposition. The minimum Stokes number for which particle inertia became significant was approximately $St_k = 1.0 \times 10^{-5}$ (Fig. 9), which translates to a 90 nm aerosol under resting conditions (15 L/min) and 50 nm particle under moderate activity conditions (30 L/min).
4. A new Sherwood number correlation was developed for mass transfer in the nasal airway that considers the concurrent actions of inertia and diffusion and is applicable for all submicrometer aerosols (Fig. 10 and Eq. (24)). An alternative correlation that can directly account for submicrometer particle deposition was also proposed (Eq. (25)).
5. Based on the results of this study, the novel DF-VC approach appeared to capture the effects of inertia in submicrometer particle deposition and to provide a more effective and computationally efficient approach for simulating respiratory aerosols in human nasal airways compared with the CS and Lagrangian tracking models.

Acknowledgements

This work was sponsored by Philip Morris USA. Dr. Julia Kimbell of the Hamner Institutes for Health Sciences is gratefully acknowledged for providing the MRI tracing data used for construction of the nasal cavity model and for helpful discussions.

References

[1] W.G. Kreyling, M. Semmler-Behnke, W. Moller, Ultrafine particle–lung interactions: does size matter?, J Aerosol Med. 19 (2006) 74–83.
[2] W.G. Kreyling, M. Semmler, W. Moller, Dosimetry and toxicology of ultrafine particles, J. Aerosol Med. 17 (2) (2004) 140–152.
[3] N. Li, C. Sioutas, A. Cho, D. Schmitz, C. Misra, J. Sempf, M.Y. Wang, T. Oberley, J. Froines, A. Nel, Ultrafine particulate pollutants induce oxidative stress and mitochondrial damage, Environ. Health Persp. 111 (4) (2003) 455–460.
[4] G. Oberdorster, M.J. Utell, Ultrafine particles in the urban air: to the respiratory tract and beyond, Environ. Health Persp. 110 (8) (2002) 440–441.
[5] D.B. Kittelson, Engines and nanoparticles: a review, J. Aerosol Sci. 29 (5–6) (1998) 575–588.
[6] G.M. Bernstein, A review of the influence of particle size, puff volume, and inhalation pattern on the deposition of cigarette smoke particles in the respiratory tract, Inhal. Toxicol. 16 (2004) 675–689.
[7] C.H. Keith, Particle size studies on tobacco smoke, Beitr. Tabakforsch. 11 (3) (1982) 123–131.
[8] ICRP, Human Respiratory Tract Model for Radiological Protection, Elsevier Science Ltd., New York, 1994.
[9] G.L. Mandell, J.E. Bennett, R.D. Bolin, Principles and Practices of Infectious Diseases, sixth ed., Churchill Livingstone, New York, 2004.
[10] V.J. Feron, J.H.E. Arts, C.F. Kuper, P.J. Slootweg, R.A. Woutersen, Health risks associated with inhaled nasal toxicants, Crit. Rev. Toxicol. 31 (2001) 313–347.
[11] J.D. Suman, B.L. Laube, R. Dalby, Validity of in vitro tests on aqueous spray pumps as surrogates for nasal deposition, absorption, and biologic response, J. Aerosol Med. 19 (4) (2006) 510–521.
[12] US FDA, Draft Guidance for Industry: Bioavailability and Bioequivalence Studies for Nasal Aerosols and Nasal Sprays for Local Action, US Food and Drug Administration, Washington, DC, 2003.
[13] H. Shi, C. Kleinstreuer, Z. Zhang, Laminar airflow and nanoparticle or vapor deposition in a human nasal cavity model, J. Biomech. Eng. 128 (2006) 697–706.
[14] L. Illum, Nasal drug delivery: new developments and strategies, Drug Deliv. Today 7 (2002) 1184–1189.
[15] A. Minn, S. Leclerc, J.-M. Heydel, A.-L. Minn, C. Denizot, M. Cattarelli, P. Netter, D. Gradinaru, Drug transport into the mammalian brain: the nasal pathway and its specific metabolic barrier, J. Drug Target. 10 (4) (2002) 285–296.
[16] K.H. Cheng, Y.S. Cheng, H.C. Yeh, R.A. Guilmette, S.Q. Simpson, S.Q. Yang, D.L. Swift, In vivo measurements of nasal airway dimensions and ultrafine aerosol depositing in human nasal and oral airways, J. Aerosol Sci. 27 (1996) 785–801.
[17] D.L. Swift, J.C. Strong, Nasal deposition of ultrafine 218Po aerosols in human subjects, J. Aerosol Sci. 27 (7) (1996) 1125–1132.
[18] Z. Lee, M.S. Berridge, PET imaging-based evaluation of aerosol drugs and their delivery devices: nasal and pulmonary studies, IEEE Trans. Med. Imag. 21 (2002) 1324–1331.
[19] Y.S. Cheng, Aerosol deposition in the extrathoracic region, Aerosol Sci. Technol. 37 (2003) 659–671.
[20] Y.S. Cheng, Y.F. Su, H.C. Yeh, D.L. Swift, Deposition of thoron progeny in human head airways, Aerosol Sci. Technol. 18 (1993) 359–375.
[21] Y.S. Cheng, Y. Yamada, H.C. Yeh, D.L. Swift, Diffusional deposition of ultrafine aerosols in a human nasal cast, J. Aerosol Sci. 19 (1988) 741.
[22] L. Gradon, C.P. Yu, Diffusional particle deposition in the human nose and mouth, Aerosol Sci. Technol. 11 (1989) 213–220.
[23] R.A. Guilmette, Y.S. Cheng, H.C. Yeh, D.L. Swift, Deposition of 0.005–12 μm monodisperse particles in a computer-milled, MRI-based nasal airway replica, Inhal. Toxicol. 6 (Suppl. 1) (1994) 395–399.
[24] J.T. Kelly, B. Asgharian, J.S. Kimbell, B. Wong, Particle deposition in human nasal airway replicas manufactured by different methods. Part II: Ultrafine particles, Aerosol Sci. Technol. 38 (2004) 1072–1079.
[25] Y. Yamada, Y.S. Cheng, H.C. Yeh, D.L. Swift, Inspiratory and expiratory deposition of ultrafine particles in a human nasal cast, Inhal. Toxicol. 1 (1988) 1–11.
[26] Y.S. Cheng, H.C. Yeh, R.A. Guilmette, S.Q. Simpson, K.H. Cheng, D.L. Swift, Nasal deposition of ultrafine particles in human volunteers and its relationship to airway geometry, Aerosol Sci. Technol. 25 (3) (1996) 274–291.
[27] J.T. Kelly, B. Asgharian, J.S. Kimbell, B. Wong, Particle deposition in human nasal airway replicas manufactured by different methods. Part I: Inertial regime particles, Aerosol Sci. Technol. 38 (2004) 1063–1071.
[28] Y. Liu, E.A. Matida, J. Gu, M.R. Johnson, Numerical simulation of aerosol deposition in a 3-D human nasal cavity using RANS, RANS/EIM, and LES, Aerosol Sci. 38 (2007) 683–700.
[29] T.B. Martonen, Z.Q. Zhang, G. Yue, C.J. Musante, Fine particle deposition within human nasal airways, Inhal. Toxicol. 15 (4) (2003) 283–303.
[30] J.D. Schroeter, C.J. Musante, D.M. Hwang, R. Burton, R. Guilmette, T.B. Martonen, Hygroscopic growth and deposition of inhaled secondary cigarette smoke in human nasal pathways, Aerosol Sci. Technol. 34 (1) (2001) 137–143.
[31] G. Yu, Z. Zhang, R. Lessmann, Fluid flow and particle diffusion in the human upper respiratory system, Aerosol Sci. Technol. 28 (1998) 146.
[32] P. Zamankhan, G. Ahmadi, Z. Wang, P.K. Hopke, Y.S. Cheng, W.C. Su, D. Leonard, Airflow and deposition of nano-particles in a human nasal cavity, Aerosol Sci. Technol. 40 (2006) 463–476.
[33] E.A.C. Hubal, J.S. Kimbell, P.S. Fedkiw, Incorporation of nasal-lining mass-transfer resistance into a CFD model for prediction of ozone dosimetry in the upper respiratory tract, Inhal. Toxicol. 8 (9) (1996) 831–857.
[34] P.W. Scherer, K. Keyhani, M.M. Mozell, Nasal dosimetry modeling for humans, Inhal. Toxicol. 6 (1994) 85–97.
[35] K. Zhao, P.W. Scherer, S.A. Hajiloo, P. Dalton, Effects of anatomy on human nasal air flow and odorant transport patterns: implications for olfaction, Chem. Senses 29 (5) (2004) 365–379.
[36] P.W. Longest, J. Xi, Computational investigation of particle inertia effects on submicron aerosol deposition in the respiratory tract, J. Aerosol Sci. 38 (1) (2007) 111–130.
[37] J. Xi, P.W. Longest, Effects of oral airway geometry characteristics on the diffusional deposition of inhaled nanoparticles, ASME J. Biomech. Eng. 130 (2008) 011008.
[38] P.W. Longest, J. Xi, Effectiveness of direct Lagrangian tracking models for simulating nanoparticle deposition in the upper airways, Aerosol Sci. Technol. 41 (2007) 380–397.
[39] Z. Zhang, C. Kleinstreuer, J.F. Donohue, C.S. Kim, Comparison of micro- and nano-size particle depositions in a human upper airway model, J. Aerosol Sci. 36 (2) (2005) 211–233.
[40] S.K. Friedlander, Smoke, Dust and Haze: Fundamentals of Aerosol Dynamics, second ed., Oxford University Press, New York, 2000.
[41] P.W. Longest, M.J. Oldham, Numerical and experimental deposition of fine respiratory aerosols: development of a two-phase drift flux model with near-wall velocity corrections, J. Aerosol Sci. 39 (2008) 48–70.
[42] L.S. Fan, C. Zhu, Principles of Gas–Solid Flows, Cambridge University Press, UK, 1998.
[43] M. Manninen, V. Taivassalo, S. Kallio, On the Mixture Model for Multiphase Flow, VTT Publicationsx, 288, Technical Research Center of Finland, 1996.
[44] J.R. Wheatley, T.C. Amis, L.A. Engel, Oronasal partitioning of ventilation during exercise in humans, J. Appl. Physiol. 71 (2) (1991) 546–551.
[45] R.A. Guilmette, J.D. Wicks, R.K. Wolff, Morphometry of human nasal airways in vivo using magnetic resonance imaging, J. Aerosol Med. 2 (4) (1989) 365–377.
[46] K.H. Cheng, Y.S. Cheng, H.C. Yeh, D.L. Swift, Deposition of ultrafine aerosols in the head airways during natural breathing and during simulated breath-holding using replicate human upper airway casts, Aerosol Sci. Technol. 23 (3) (1995) 465–474.
[47] J.D. Schroeter, J.S. Kimbell, B. Asgharian, Analysis of particle deposition in the turbinate and olfactory regions using a human nasal computational fluid dynamics model, J. Aerosol Med. 19 (3) (2006) 301–313.
[48] N. Mirza, H. Kroger, R.L. Doty, Influence of age on the 'nasal cycle', Laryngoscope 107 (1) (1997) 62–66.
[49] M. Ohki, T. Ogoshi, T. Yuasa, K. Kawano, M. Kawano, Extended observation of the nasal cycle using a portable rhinoflowmeter, J. Otolaryngol. 34 (5) (2005) 346–349.
[50] T.L. Chan, R.M. Schreck, M. Lippmann, Effect of the laryngeal jet on particle deposition in the human trachea and upper bronchial airways, J. Aerosol Sci. 11 (1980) 447–459.
[51] J. Xi, P.W. Longest, Transport and deposition of micro-aerosols in realistic and simplified models of the oral airway, Ann. Biomed. Eng. 35 (4) (2007) 560–581.
[52] P.W. Longest, S. Vinchurkar, Validating CFD predictions of respiratory aerosol deposition: effects of upstream transition and turbulence, J. Biomech. 40 (2007) 305–316.
[53] D.C. Wilcox, Turbulence Modeling for CFD, second ed., DCW Industries Inc., California, 1998.
[54] M.D. Allen, O.G. Raabe, Slip correction measurements of spherical solid aerosol particles in an improved Millikan apparatus, Aerosol Sci. Technol. 4 (1985) 269–286.
[55] W.C. Hinds, Aerosol Technology: Properties, Behavior, and Measurement of Airborne Particles, John Wiley and Sons, New York, 1999.
[56] I. Balashazy, W. Hofmann, T. Heistracher, Computation of local enhancement factors for the quantification of particle deposition patterns in airway bifurcations, J. Aerosol Sci. 30 (1999) 185–203.
[57] B.S. Cohen, J.Q. Xiong, C.P. Fang, W. Li, Deposition of charged particles on lung airways, Health Phys. 74 (1998) 554–560.
[58] K. Keyhani, P.W. Scherer, M.M. Mozell, Numerical simulation of airflow in the human nasal cavity, J. Biomech. Eng. – Trans. ASME 117 (4) (1995) 429–441.
[59] R.P. Subramaniam, R.B. Richardson, K.T. Morgan, J.S. Kimbell, R.A. Guilmette, Computational fluid dynamics simulations of inspiratory airflow in the human nose and nasopharynx, Inhal. Toxicol. 10 (2) (1998) 91–120.
[60] R. Fodil, L. Brugel-Ribere, C. Croce, G. Sbirlea-Apiou, C. Larger, J.F. Papon, C. Delclaux, A. Coste, D. Isabey, B. Louis, Inspiratory flow in the nose: a model

coupling flow and vasoerectile tissue distensibility, J. Appl. Physiol. 98 (1) (2005) 288–295.
[61] G.P. Bridger, Physiology of nasal valve, Arch. Otolaryngol. 92 (6) (1970) 543–553.
[62] G.P. Bridger, D.F. Proctor, Maximum nasal inspiratory flow and nasal resistance, Ann. Otol. Rhinol. Laryngol. 79 (3) (1970) 481–486.
[63] O. Hilberg, F.T. Jensen, O.F. Pedersen, Nasal airway geometry: comparison between acoustic reflections and magnetic resonance scanning, J. Appl. Physiol. 75 (6) (1993) 2811–2819.
[64] D.N. Pickering, C.S. Beardsmore, Nasal flow limitation in children, Pediatr. Pulmonol. 27 (1) (1999) 32–36.